Cell Reports
Article

Higher-Order Architecture of Cell Adhesion Mediated by Polymorphic Synaptic Adhesion Molecules Neurexin and Neuroligin

Hiroki Tanaka,[1] Naoyuki Miyazaki,[1,2] Kyoko Matoba,[1,2] Terukazu Nogi,[3] Kenji Iwasaki,[1,2] and Junichi Takagi[1,*]
[1]Laboratory of Protein Synthesis and Expression, Institute for Protein Research, Osaka University, 3-2 Yamadaoka, Suita, Osaka 565-0871, Japan
[2]Core Research for Evolutional Science and Technology, Science and Technology Agency, Suita 565-0871, Japan
[3]Department of Supramolecular Biology, Graduate School of Nanobioscience, Yokohama City University, 1-7-29 Suehiro-cho, Tsurumi-ku, Yokohama 230-0045, Japan
*Correspondence: takagi@protein.osaka-u.ac.jp
http://dx.doi.org/10.1016/j.celrep.2012.06.009

SUMMARY

Polymorphic adhesion molecules neurexin and neuroligin (NL) mediate asymmetric *trans*-synaptic adhesion, which is crucial for synapse development and function. It is not known whether or how individual synapse function is controlled by the interactions between variants and isoforms of these molecules with differing ectodomain regions. At a physiological concentration of Ca^{2+}, the ectodomain complex of neurexin-1 β isoform (Nrx1β) and NL1 spontaneously assembled into crystals of a lateral sheet-like superstructure topologically compatible with transcellular adhesion. Correlative light-electron microscopy confirmed extracellular sheet formation at the junctions between Nrx1β- and NL1-expressing nonneuronal cells, mimicking the close, parallel synaptic membrane apposition. The same NL1-expressing cells, however, did not form this higher-order architecture with cells expressing the much longer neurexin-1 α isoform, suggesting a functional discrimination mechanism between synaptic contacts made by different isoforms of neurexin variants.

INTRODUCTION

Synaptic junctions between axons and dendrites are formed across the 20-nm-wide synaptic cleft by cell adhesion machinery from both sides (Dalva et al., 2007). Although several homophilic adhesion molecules are involved in the process of synapse formation and maintenance, the asymmetric nature of synapses underscores the importance of heterophilic adhesion molecules, represented by the presynaptic neurexins (Nrxs) and the postsynaptic neuroligins (NLs) (Südhof, 2008). Humans have three Nrx genes (Nrx1–Nrx3), each of which expresses either a longer (~1,500 aa) α- or a shorter (~400 aa) β-Nrx based on differential promoter usage. The presence of five alternative splicing sites (SS1–SS5) further diversifies the Nrx isoforms expressed in the brain (Missler and Südhof, 1998). Similarly, NLs are encoded by four separate genes giving rise to NL1–NL4, all of which have at least two alternatively spliced transcripts (Lisé and El-Husseini, 2006). Genetic, transcriptional, and translational mechanisms exist, therefore, to ensure the production of large number of variants/isoforms for both proteins. Although all Nrxs have the potential to bind to any NL to some degree (Koehnke et al., 2010), it is currently believed that complex "splice codes" fine-tune the interaction specificity between Nrx and NL isoforms (Boucard et al., 2005; Chih et al., 2006; Comoletti et al., 2006). Furthermore, each Nrx isoform shows differential distribution in different classes of neurons (Ullrich et al., 1995), suggesting a functional specification of neurons and/or synapses that depends on the unique Nrx/NL adhesion machinery being used.

The unique property of the Nrx/NL adhesion system is that it is a "signaling" device rather than a simple physical support of the synaptic cell-cell contacts, in that transcellular engagement between Nrx and NL ectodomains can induce intracellular pre- and postsynaptic specializations on their respective sides (Graf et al., 2004; Scheiffele et al., 2000). Both Nrx and NL possess a PDZ binding motif at the C-terminal of their cytoplasmic tail, which is known to bind synapse-specific proteins such as CASK and PSD-95 (Dean and Dresbach, 2006). If and how an extracellular protein-protein engagement alone can eventually result in an intracellular protein recruitment, however, remain unanswered.

For the Nrx and NL ectodomain regions, multiple crystal structures have been solved for each partner, both in solitary (before adhesion) (Chen et al., 2011; Koehnke et al., 2008, 2010; Miller et al., 2011; Rudenko et al., 1999; Sheckler et al., 2006; Shen et al., 2008; Tanaka et al., 2011) and in complex (after adhesion) (Araç et al., 2007; Chen et al., 2008; Fabrichny et al., 2007). They cover many of the different types (Nrx1–Nrx3, NL1–NL4), different isoforms (α- and β-Nrx), and different variants (with and without some of the SS insertions), and resulted in a tremendous amount of information regarding the recognition specificity at the level of amino acid residues. These high-resolution structures of isolated molecules, however, provide little information about the structural and topological organization of the adhesion machinery specific for each isoform/variant in the context of the real cell-cell junction.

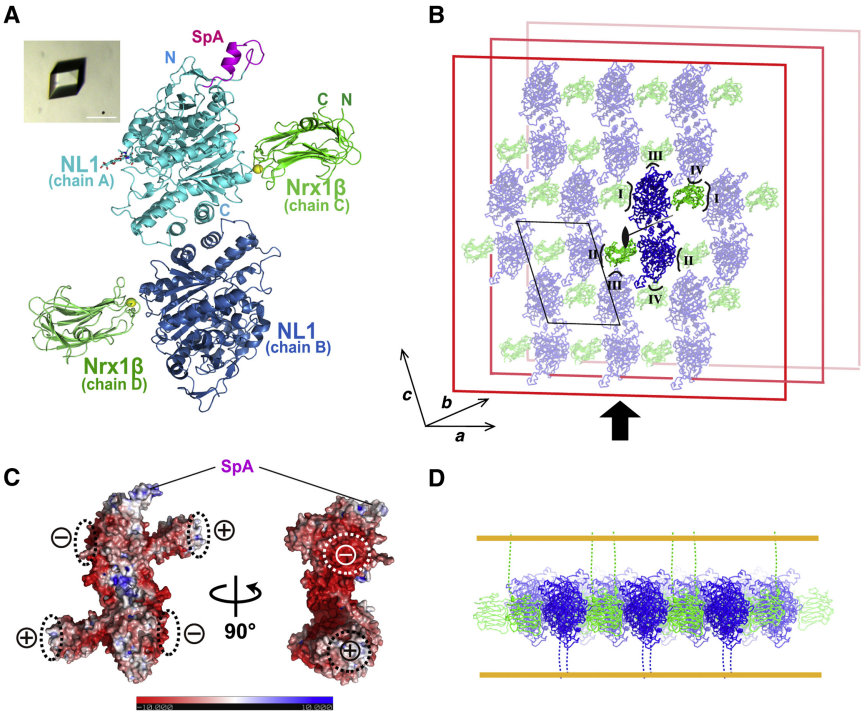

Figure 1. The 2D Assembly of the Nrx1β-NL1 Complex in the Crystal

(A) Structure of the Nrx1β-NL1A^{+}B^{-} 2:2 complex, with each chain colored differently and SpA shown in magenta. Inset is crystal of the complex obtained in a Ca^{2+}-containing buffer. Scale bar, 400 μm.

(B) Packing interactions are illustrated. In the crystal, Nrx1β-NL1 hetrotetramers are packed laterally via a set of interfaces (interfaces I–IV) to make sheets (red frames) that stack on top of each other along the unit cell *b* axis. For clarity only the front sheet is shown, and only one complex unit is shown in dark color.

(C) Electrostatic surface of the Nrx1β-NL1A^{+}B^{-} hetrotetramer with a contour level of ±10 kT/e shown in two different views. Surfaces comprising interfaces I and II (dashed circles) are marked with their overall electrostatic property (+ or −).

(D) Hypothetical model of the *trans*-synaptic Nrx1β-NL1 adhesion architecture is shown. The sheet-like assembly of Nrx1β (green)-NL1 (blue) complexes is viewed from the direction indicated by an arrow in (B), with their C-terminal "stalk" connecting to the presynaptic and postsynaptic membranes (gold lines) represented by dashed lines.

See also Figure S1.

We first set out to investigate the effect of splice site A (SpA) insertion on the NL1 structure by crystallizing the ectodomain complex between the "A^{+}" variant of NL1 and Nrx1β without the splice insertion 4 sequence (often referred to as Nrx1βΔ, but called Nrx1β throughout this article for simplicity). Although we succeeded in visualizing the inserted A segment in the NL1 crystal structure, the resultant NL1A^{+}:Nrx1β complex structure was indifferent from those of NL1A^{-}:Nrx1β complexes reported previously. We unexpectedly found, however, a "layer" formation by the laterally assembled Nrx/NL complexes in an unusual Ca^{2+}-induced crystal. Correlative light-electron microscopy (CLEM) combined with a high-pressure freezing/freeze substitution technique revealed that a similar layer was formed at the junction between cells expressing NL1-enhanced green fluorescent protein (EGFP) and DsRed-tagged Nrx1β (Nrx1β-DsRed). Such a layer was not formed when Nrx1α-expressing cells were used, indicating that the same NL-bearing cells develop different types of synapse-like structures in response to α as opposed to β-Nrx engagement.

RESULTS

Structure of Nrx1β/NL1A^{+} Ectodomain Complex

Ectodomain fragments of NL1 with SpA insertion and Nrx1β were each purified to homogeneity, concentrated, and mixed together at an equimolar concentration in a Tris buffer (pH 8.0). Unexpectedly, the sample spontaneously developed crystalline precipitates immediately after the mixture was supplemented with ~2 mM $CaCl_2$. Microscopic observation revealed that the precipitates consisted of microcrystals, which eventually grew to diffraction-quality crystals (Figure 1A, inset). The crystal structure of the Nrx1β/NL1 complex determined at 3.3 Å resolution comprises a heterotetramer in which two Nrx1β protomers bind to distal ends of a NL1 homodimer (Figure 1A; Table 1). This 2:2 arrangement, as well as the recognition mode that involves intermolecular hydrogen-bonding network and Nrx1β-bound Ca^{2+} (Figure S1A), is identical to that seen in the previously reported crystal structures of Nrx1β/NL1 (Araç et al., 2007; Chen et al., 2008) and Nrx1β/NL4 (Fabrichny et al., 2007) complexes. Moreover, we could see clear electron density for SpA insertion in one of the NL1 molecules (Figure S1B). SpA protrudes from the globular acetylcholinesterase-like domain of NL1 into solution and adopts a unique conformation containing a short α helix (Figure 1A). Because we did not see clear electron density corresponding to this segment in the other molecule (chain B), it is possible that SpA exists as a rigid structured unit in the physiological state but can wobble at the base of the protrusion. Importantly, comparison with the structure of the previously reported "A^{-}" version of NL1 reveals that the insertion of this segment does not cause any conformational rearrangements in the surrounding residues. Furthermore, SpA is positioned away from the Nrx1β/NL1 interface, and it is not located at the lateral association interface, which will be described in the next section. Alternative insertion of this segment in NL1 expressed on cell surface, therefore, does not seem to directly affect the adhesive function of NL1 toward cells expressing Nrx1β.

Two-Dimensional Assembly of the Nrx1β/NL1 Complexes

Although the structure of the individual Nrx1β/NL1 complexes in our crystal is essentially identical to those of previous reports, the packing interaction in the crystal is highly unique: the 2:2

Table 1. Summary of Data Collection and Refinement Statistics

Data Collection Statistics	
Space group	$P2_1$
Cell dimensions	
a, *b*, *c* (Å)	81.26, 95.18,120.40
β (°)	108.6
X-ray source	PF BL-17A
Wavelength (Å)	1.00000
Resolution (Å)	48.9–3.30 (3.48–3.30)
No. of reflections	
Observed	94,570 (13,066)
Unique	25,519 (3,541)
Completeness (%)	97.3 (93.7)
Redundancy	3.7 (3.7)
R_{merge}	8.9 (31.1)
$<I/\sigma(I)>$	13.2 (4.3)
Refinement Statistics	
Resolution (Å)	48.9–3.3
No. of reflections used	
Working set/test set	22,921/2,586
R_{work}/R_{free} (%)	20.5/28.7
No. of atoms	
Protein	11,253
Sugar	67
Ion	2
Averaged *B* factors (Å^2)	
Protein	66.3
Sugar	100.8
Ion	69.3
Rmsd from ideality	
Bond length (Å)	0.007
Bond angles (°)	1.05
Ramachandran plot (MolProbity)	
Favored (%)	92.61
Outlier (%)	0.63

complexes are regularly assembled into a plane parallel to the crystallographic *a* and *c* axes, and the resultant sheet-like structures stack along the *b* axis to make the three-dimensional crystal (Figure 1B). Within this "sheet," one complex interacts with two packing mates along the *a* axis using two interfaces (interface I and II) and two more mates along the *c* axis using smaller interfaces (interface III and IV) (Figure 1B). Interfaces I and II are quasi-equivalent to each other and are formed between a Nrx1β in one complex and a NL1 from a neighbor, with both interactions facilitated by the electrostatically complementary molecular surfaces located opposite to the Ca^{2+}-mediated primary recognition sites (Figure 1C). Furthermore, the 2:2 arrangement of the complex reinforces the simultaneous side-by-side formation of these interactions, creating a positive cooperativity for the lateral propagation of the assembly (Figure 1C). We note that very similar packing interaction was present in the Nrx1β/NL4 complex crystal reported by Fabrichny et al. (2007), although the resultant linear array of complexes did not associate horizontally to make two-dimensional (2D) sheet. The most important aspect of the sheet structure is that all the complexes within a sheet align with their internal 2-fold symmetry axis running normal to the sheet (i.e., parallel to the *b* axis), resulting in the C termini of Nrx1β and NL1 all projecting away from the sheet but pointing toward opposite directions. Because the C termini in both proteins connect to the transmembrane domain, this organization is topologically compatible with the situation at a synaptic cleft where Nrx1β and NL1 each protrude from opposing cell membranes to form *trans*-synaptic adhesion (Figure 1D). The fact that our crystal (and hence the 2D sheet therein) was spontaneously formed in a condition close to that of the physiological extracellular milieu gave us reason to speculate that this 2D sheet-like assembly may also be formed at the synaptic junction.

Intercellular Adhesion Structure Mediated by Nrx1β and NL1

We next imaged cell-cell junctions using both light and electron microscopy (EM). It has been reported that non-neuronal cells heterologously expressing Nrx1β and NL1 undergo heterotypic cell-cell aggregation in a Ca^{2+}-dependent manner (Dean et al., 2003). Thus, HEK293T cells were stably transfected with either DsRed-tagged Nrx1β (Nrx1β-DsRed) or EGFP-tagged NL1 (NL1-EGFP). For this experiment we used the NL1 variant containing both A and B insertions because it is the major form expressed in the brain (Chih et al., 2006). When a mixture of these cells was suspended in media containing 2 mM Ca^{2+} and incubated for 30 min at room temperature, spontaneous cell-cell aggregate formation was observed (Figure 2A). Fluorescence images show that the cell-cell aggregation occurred preferentially between differently colored cells, indicating that the adhesion is mediated by the transcellular engagements between Nrx1β and NL1. Furthermore, strong accumulation and colocalization of Nrx1β-DsRed and NL1-EGFP at the cell contact sites were revealed by confocal imaging (Figure 2B). Next, we aimed at characterizing the adhesion structure formed between cells at molecular resolution using EM. To prepare EM specimen, the heterotypic cell-cell aggregates were subjected to high-pressure freezing followed by dehydration using a freeze substitution method to maximally preserve fine ultrastructure (Brown et al., 2009; Verkade, 2008). Figure 2C shows a representative EM image of the cell-cell junction formed between Nrx1β and NL1-expressing cells. At 40,000× magnification, the two opposing cell membranes at the cell-cell junction appeared as smooth, parallel lines separated by ~30 nm, with an electron-dense midline at the center (Figures 2C and S2). The midline is ~7 nm thick, runs parallel to the plasma membranes, and is largely continuous, although small gaps (<10 nm) are frequently visible. We believe that this midline density corresponds to an extracellular adhesion structure made of laterally clustered ectodomain complexes of Nrx1β and NL1A$^+$B$^+$ because it is invariably present at regions where two cell membranes make close and parallel apposition compatible with the transcellular molecular interaction but disappears when the intermembrane distance becomes larger than 30 nm (Figure 2C, indicated by arrowhead; see also Figure 3 for more examples). No such

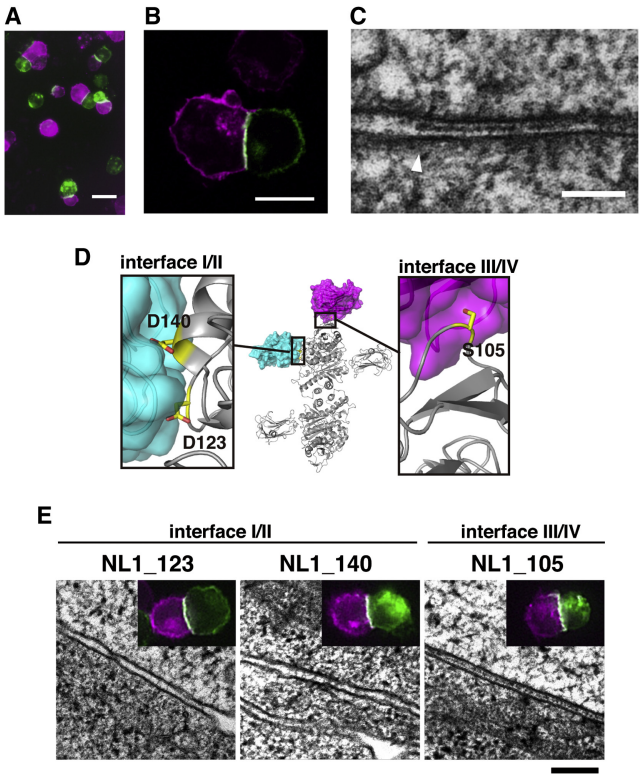

Figure 2. Cell-Cell Contact Sites Involving Transcellular Binding between Nrx1β and NL1

Aggregates formed between cells expressing NL1A$^+$B$^+$-EGFP (green) and Nrx1β-DsRed (magenta) were imaged by (A) epifluorescence or (B) confocal microscopy.

(C) High-magnification EM image of the cell adhesion structure formed between NL1A$^+$B$^+$ and Nrx1β is presented.

(D) Mutational design is demonstrated. One Nrx1β-NL1 tetrameric complex (gray ribbon model) and two Nrx1β molecules from the packing mates contacting through interface I/II (cyan) or interface III/IV (magenta) are shown. Residues located at the interfaces (yellow stick models) were chosen for the glycosylation mutation to disrupt each interaction.

(E) Effect of the NL1 mutations on the morphology of the cell-cell junction is illustrated. Representative EM images of the heterotypic cell adhesion sites formed between Nrx1β-DsRed cells and mutant NL1A$^+$B$^+$-EGFP cells are shown. Insets are merged epifluorescence images of heterotypic cell-cell aggregate for each mutant NL1.

Scale bars, 20 μm (A and B) and 100 nm (C and E).

See also Figure S2.

densities were observed at homotypic cell-cell contact regions with a distance of ~30 nm or less that are occasionally found in samples consisting solely of parental HEK293T, Nrx1β-DsRed-expressing, or NL1-EGFP-expressing cells (data not shown), ruling out the possibility that it is caused by a staining artifact.

Next we asked, through mutational experiments, if the lattice-like lateral packing between the 2:2 NL1-Nrx1β ectodomain complexes seen in the crystal plays an essential role in the formation of the "midline density." Three NL1 residues at the heart of interfaces I/II (D123 or D140) or III/IV (S105) (Figure 2D) were mutated to harbor an N-glycosylation signal (N-X-T/S), presuming that the presence of a large glycan chain would disrupt the intertetramer interactions. Mutations were introduced in the context of the NL1A$^+$B$^+$-EGFP, and stable cell clones expressing at roughly the same level were established for each mutant (Figure S2). All mutant NL1-EGFPs were able to mediate efficient cell aggregation with Nrx1β-DsRed, with no macroscopic difference in the fluorescence colocalization at the cell contact sites (Figure 2E, insets). EM observation of the cell-cell junctions, however, revealed that the two interface I/II mutations resulted in a drastically different morphology compared to the wild-type: the two apposing membranes appeared as rough lines with uneven spacing, and the extent of the accumulation of the extracellular materials was much less pronounced compared to the densely packed "midline" (Figures 2E, with more examples in Figure S2). This result strongly supports the notion that the higher-order assembly of the NL1-Nrx1β ectodomain complex found in the crystal packing can be formed in the physiological cell-cell junctions and that such structure requires more than a random accumulation of intercellular adhesion complexes. In contrast, mutational disruption of interface III/IV at S105 did not cause any obvious morphological change, indicating that this small interface has a much less specific contribution to the higher-order assembly.

One caveat to our observation is that the EM images were taken separately from the fluorescence microscopy images and are not directly correlated to a particular heterotypic cell-cell contact. More importantly, the fixed, stained specimens no longer fluoresce, making it impossible to tell the sidedness of the contact. We therefore employed CLEM, a novel method for high-resolution imaging of target structures without loss of fluorescence information (Plitzko et al., 2009; Polishchuk et al., 2000). The CLEM procedure involves (1) live-cell image recording on a sapphire glass disc at the bottom of specimen carrier overlaid with a specially patterned grid, (2) high-pressure freezing of the sample, (3) dehydration by freeze substitution and resin embedding, and (4) sectioning and examination by EM (reviewed in McDonald, 2009; for details, see Experimental Procedures and Figure S3). Using this technology, cell-cell junctions between Nrx1β-DsRed- and NL1A$^+$B$^+$-EGFP-expressing cells located by fluorescence microscopy were correlated to the corresponding fields in the fixed specimens and were imaged by EM (Figure 3A, three CLEM series are shown). The resultant EM images further confirmed the characteristic morphology of the heterotypic adhesion sites, showing the midline density along the closely aligned smooth membranes. We also performed CLEM analysis using cells expressing NL1A$^+$B$^-$-EGFP. This variant of NL1 lacking the nine-residue insertion at the splice site B (SpB) is expressed at lower levels in the brain (Chih et al., 2006), but it is expected to have distinct function because it can bind to Nrx1α (Boucard et al., 2005). As shown in Figure 3B, NL1A$^+$B$^-$-EGFP-expressing cells underwent strong cell aggregation with Nrx1β-DsRed-expressing cells, and the electron dense midline was clearly observed at the cell-cell contact sites. These results indicate that the sheet-like adhesion structure can be formed regardless of the SpB insertion in NL1.

CLEM technology also enabled us to definitively tell the sidedness of the cell contacts. Thus, a closer inspection of the cell-cell junction in the high-magnification micrographs revealed that the midline is not positioned at the center of the membrane cleft.

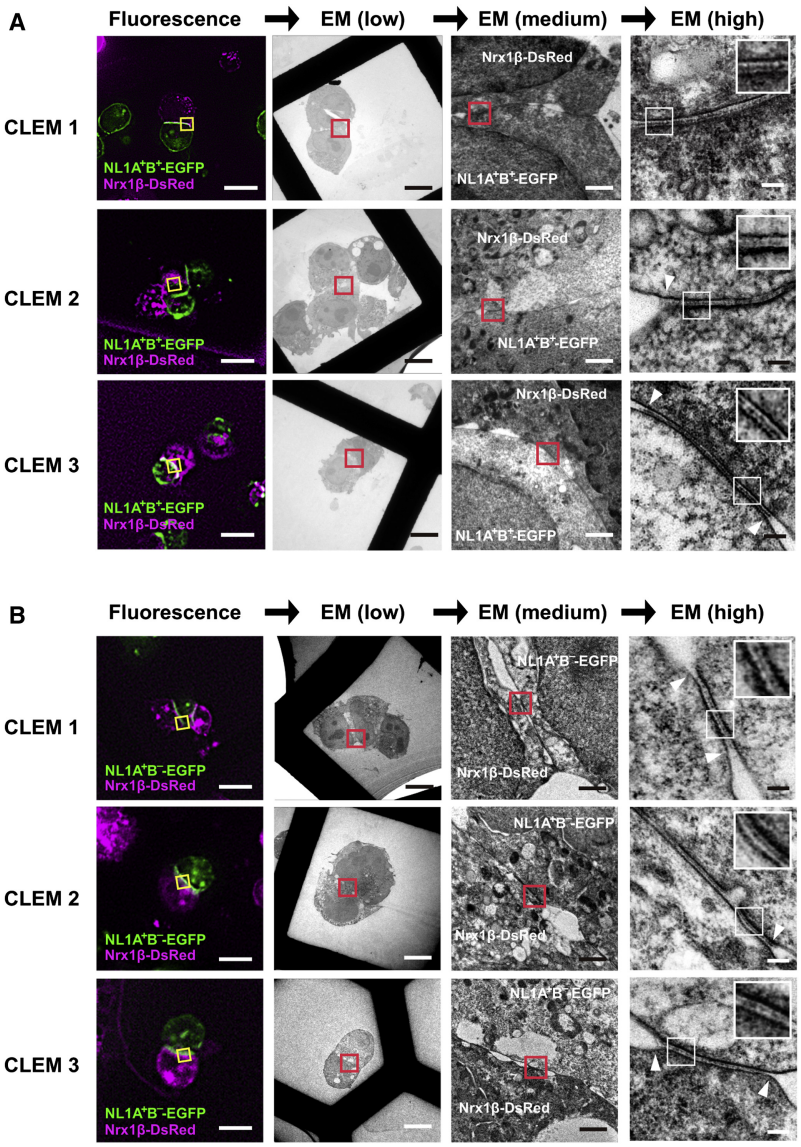

Figure 3. Visualization of Cell-Cell Contact Sites Mediated by Nrx1β-NL1 Interactions Using CLEM

Three different CLEM series are shown for contact sites formed between Nrx1β-DsRed cells and NL1A$^+$B$^+$-EGFP cells (A) or NL1A$^+$B$^-$-EGFP cells (B). Fluorescence micrographs (far left) are correlated with the low-magnification TEM images (second from left), followed by intermediate (second from right) and high magnifications (far right). The yellow box in the fluorescence images corresponds to the region shown in the low-magnification TEM images, and the areas indicated by the red box in the low- and intermediate-magnification images correspond to that shown in the intermediate- and high-magnification images, respectively. In the high-magnification images, regions with membrane apposition containing a clear "midline" (white box) are further magnified and shown as inset. The boundary between the area with close membrane apposition and that with wider separation is marked by a white arrowhead. Scale bars are 20 μm for fluorescence and low-magnification EM images, 1 μm for intermediate-magnification, and 100 nm for high-magnification images. See also Figure S3.

Instead, it always lies closer to the membrane bearing NL1. Figure 4A shows the density profile of the membrane cleft, demonstrating the off-centered nature of the midline. This asymmetry is consistent with the heterotypic transcellular association between two adhesion molecules that possess membrane-proximal "stalk" regions of different length (102 residues for Nrx1β and 57 residues for NL1) because gap widths between the midline density and the flanking membranes were calculated to be 9.4 and 5.7 nm for the Nrx1β- and the NL1-expressing sides, respectively. This result further supports the notion that the midline density represents the structure made by the complex between the globular portion of the ectodomains of Nrx1β and NL1.

Intercellular Adhesion Mediated by Nrx1α and NL1

Structures of the Nrx1α ectodomain fragment have been recently solved by several groups (Chen et al., 2011; Miller et al., 2011; Tanaka et al., 2011), showing that the ~1,200-residue N-terminal segment missing in Nrx1β folds into an elongated structure of a length of >120 Å. Superposition of these structures onto the 2D sheet of the Nrx1β/NL1 complex using the common LNS6 domain indicates that Nrx1α would not be able to form a 2D sheet due to steric clashes with neighbors (Figure S1C). As a consequence, it is expected that Nrx1α cannot assemble into densely packed structures upon transcellular binding with NL1, which would lead to a cell adhesion architecture quite different from that made by Nrx1β. To test this hypothesis, we imaged junctions between Nrx1α- and NL1A$^+$B$^-$-expressing cells. We isolated a HEK293T cell clone that expresses DsRed-tagged Nrx1α (Nrx1α-DsRed) on the cell surface at a similar level to that of the Nrx1β-DsRed cells used in the previous experiments (Figure S4A). Nrx1α-DsRed cells aggregated efficiently with the NL1A$^+$B$^-$-EGFP cells with clear receptor colocalization at the cell-cell contact sites (Figure 5, far-left panels, and Figure S4B), indicating that Nrx1α/NL1 can develop adhesion structure similar to that involving Nrx1β/NL1 at a macroscopic level. At higher magnification, however, the overlap between DsRed and EGFP fluorescence is less pronounced in the Nrx1α-NL1 junction compared to that of Nrx1β-NL1 (Figure S4C), suggesting wider membrane separation. This difference was unequivocally shown at even higher magnification in the EM images from the CLEM experiments performed on the cell-cell contact between Nrx1α-DsRed and NL1A$^+$B$^-$-EGFP-expressing cells (Figure 5). There are a number of important differences between the junction architecture of Nrx1α-NL1 and that of Nrx1β-NL1. First, as described above, the intermembrane distances are wider in Nrx1α-NL1 junction, measuring ~40 nm on average (Figure 4B). In addition the two apposing membranes

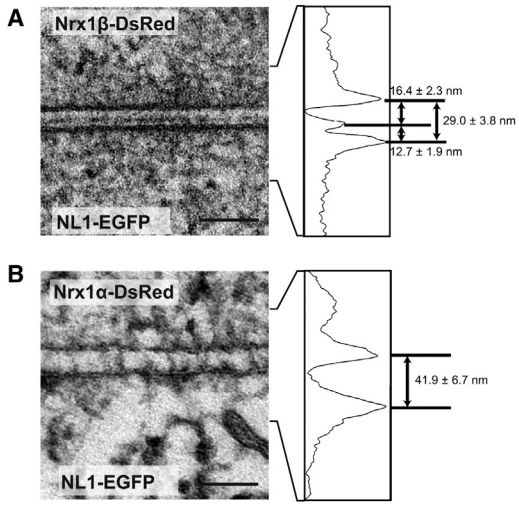

Figure 4. Intermembrane Distances at the Cell-Cell Contacts Mediated by NL-Nrx1 Interactions

From TEM images of the cell adhesion sites, regions with good membrane linearity are boxed out, and the density profiles were derived by integrating the image intensity along the longitudinal axis parallel to the membrane. A representative image and the associated density profile are shown for cell adhesion sites involving NL1-Nrx1β (A) or NL1-Nrx1α (B) interactions. Distances between the peak positions of the density profile are measured for a total of (A) 59 and (B) 26 boxed areas representing more than 30 nm of cell junction in length and are shown as mean ± SEM. Scale bars, 100 nm.

are not regularly spaced, leading to the "wavy" membranes seen in the Nrx1α-NL1 junction contrasting with the highly flat and evenly spaced membranes seen in the Nrx1β-NL1 junction. Most importantly, the electron dense midline is completely absent in the Nrx1α-NL1 junction. Instead of a midline parallel to the membranes, densities that traverse the intermembrane extracellular space are present throughout the membrane apposition area (Figure 5, far-right panels). In most cases the traversing density "bridges" the membranes by spanning the entire extracellular space, although there are no regularities in the shape of the individual bridge. Moreover, the densities are rather sparsely and irregularly distributed with no signs of lateral clustering, indicating that the Nrx1α-NL1 transcellular adhesion complexes do not assemble into the higher-order sheet-like structure found in the contact site involving Nrx1β-NL1 interactions.

DISCUSSION

Because of the overlapping distribution in tissues as well as the lack of convenient molecular probes (e.g., antibodies) that can distinguish different isoforms, it has been difficult to dissect the molecular functions of α- and β-Nrx during the development of synaptic contacts. Imaging on non-neuronal heterologously transfected cells, although nonphysiological, provided a way to analyze fine structures of the adhesion architecture in an isoform-specific manner. Furthermore, the correlation technology (i.e., CLEM) utilized here enabled convenient and straightforward molecular identification in the EM images. The results presented here clearly show that there is a fundamental difference between α- and β-Nrx in the organization of adhesion machinery when they bind to cells bearing NL1. Importantly, a sheet-like structure reminiscent of the 2D layer present in the Ca^{2+}-induced crystal of the Nrx1β/NL1 ectodomain complex was found in the extracellular space at the junctions of Nrx1β- and NL1-expressing cells. A layer of extracellular material has been frequently observed in the synaptic cleft by conventional EM (Peters et al., 1991), but these structures had been disputed as staining artifacts (Gray, 1975) until Lucić et al. imaged the synaptic contact sites using cryo-EM and confirmed the presence of proteinaceous material at the center of synaptic cleft, which was predicted to represent adhesion molecules (Lucić et al., 2005). Furthermore, Zuber et al. performed cryo-EM imaging on ultrathin vitreous sections of rat hippocampal slices, reporting periodically organized material in the synaptic cleft along the membranes (Zuber et al., 2005). Notably, the determined periodicity of the material (8.2 ± 0.4 nm) coincides with the 82 Å lattice constant of our Nrx1β/NL1 complex crystal in the *a* axis direction (which lies in the plane of the crystalline sheet), raising the possibility that the lateral assembly of β-Nrx/NL complexes may indeed exist in the real neuronal synapse. In sharp contrast to the densely packed sheet-like material at the junction between Nrx1β and NL1, the morphology of the Nrx1α-mediated adhesion sites is represented by sparsely and randomly distributed transcellular linkages with enlarged membrane distance. In the recently determined crystal structure of Nrx1α ectodomain by Chen et al. (2011) and Miller et al. (2011), the region N terminal to the LNS6 domain assumes an elongated module of ~120 Å in length, connected to LNS6 through the mobile EGF domain. This "α-specific" segment can extend in various directions, thus making the individual 2:2 complex large and conformationally heteromorphic, consistent with the observed morphology of the junction.

In addition to the difference in the isoform of Nrx, the adhesion architecture formed by transcellular Nrx-NL interactions may also be affected by the insertion/deletion of the SS segments present in both adhesion molecules. Although the presence of the SpA protrusion does not seem to affect the formation of the putative adhesion sheet when NL1 is bound by β-Nrx, its location is somewhat close to the expected position of the N-terminal segment of Nrx1α (Figure S1C), suggesting the possibility that SpA insertion/deletion may modulate the properties of Nrx1α-mediated adhesion sites by changing the orientation of the LNS1–LNS5 segment. Another intriguing question is that of the effect of SS4 insertion (within β-Nrx) on the lateral assembly of the adhesion complex. Superposition of the structure of Nrx1β(4+) determined by Koehnke et al. (2010) (PDB 3MW2) onto the Nrx1β in our sheet structure reveals that most of the SS4 protrusion can be accommodated in an open space in the lattice, but its tip approaches the NL1 in a packing mate and could potentially interfere with interface I/II (Figure S1C). It remains to be investigated whether these splice variations affect synaptic functions by changing the higher-order morphology of particular adhesion site, in addition to the fine-tuning of the recognition specificity.

The tight, ordered 2D assembly of Nrx1β/NL1 complexes presented here not only sheds light on the morphology of the

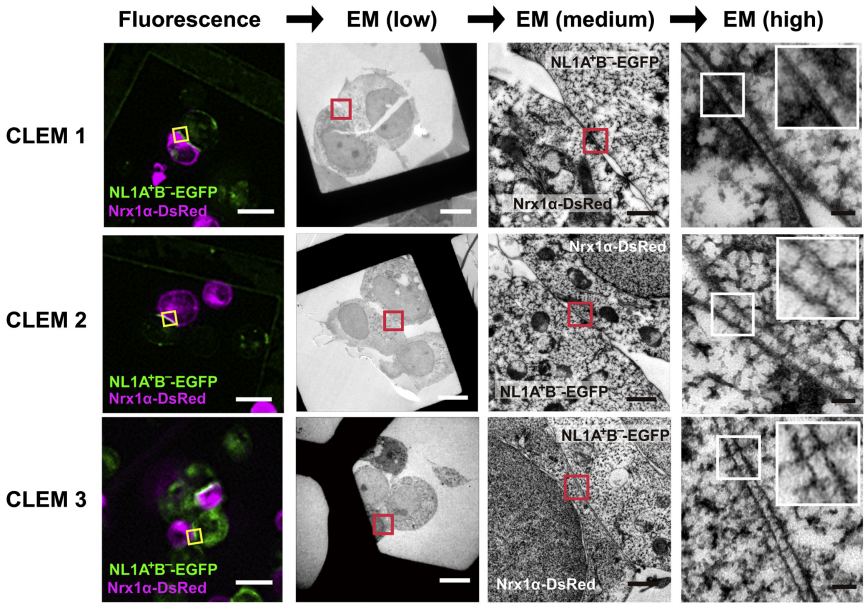

Figure 5. Visualization of Cell-Cell Contact Sites Mediated by Nrx1α-NL1 Interactions Using CLEM

Three different CLEM series are shown as in Figure 3 but using cells expressing Nrx1α-DsRed and NL1A^{+}B^{-}-EGFP. See also Figure S4.

adhesion architecture but also provides clues about the potential mechanism of signal transduction upon cell adhesion. It has been known that forced clustering of Nrx1β on neurons by multimerized but not standard divalent antibodies induces synaptic vesicle accumulation, mimicking presynaptic differentiation (Dean et al., 2003). This multimeric clustering would not be accomplished by the *trans*-synaptic engagement with dimeric NLs alone but requires lateral association of the preformed 2:2 complex. The extracellular sheet formation suggests that it is an intrinsic property of the Nrx1β/NL1 complex to spontaneously assemble into an ordered cluster without any exogeneous input, leading to signal induction at the cytoplasmic face. Importantly, this clustering does not take place until the transcellular binding occurs because the complimentary electrostatic patches are formed only after the formation of the 2:2 complex (Figure 1C). The affinity for the lateral interaction between the Nrx1β/NL1 complexes must be very low because the 2D sheet was observed only when the protein concentration was very high (i.e., crystallization conditions) or when the proteins are confined at high local concentration on a 2D membrane (i.e., on cell surface), and we could not detect any signs of oligomer formation in solution (data not shown). It is expected, therefore, that the sheet formed at the cell-cell contact site is not a permanent structure and can remodel upon cellular events, including cytoskeletal rearrangements, recruitment of other membrane proteins to the site, or ectodomain shedding of NL and/or Nrx.

Although the precise mechanism of the synapse-inducing activity of both Nrx and NL upon their engagement is still unknown, recruitment of specific pre- or postsynaptic proteins through the interaction motifs at the cytoplasmic tail of each molecule should play a major role (Dean and Dresbach, 2006). Yet, these interaction motifs, including the PDZ binding motif at the C terminus, are generally well conserved within families and are identical among different isoforms/variants that differ only in the ectodomain region. Therefore, it has been difficult to hypothesize the presence of isoform/variant-specific signaling. Our results show, however, that the cytoplasmic anchor points assembled inside the adhesion structures made by NL1 molecules on a cell would exhibit dramatically different pattern (e.g., in density and regularity) depending on the isoform of Nrx on the opposing cell surface (Figure 6). This provides a way to control the architecture of cytoplasmic signaling components from the extracellular side, which may constitute a mechanism of isoform-specific functional diversification of synapses.

The presence of the dense and ordered proteinaceous sheet radically differs from our traditional view of the synaptic cleft as an empty space. When the sheet is formed at its highest density (i.e., approximately that present in the crystal), it constitutes a membrane-like structure with a maximum pore size of ~35 Å (Figure S5). Therefore, the sheet would allow passage of small molecules but may exclude macromolecules such as secreted proteins. We also note that the electrostatic potential of the putative sheet made by Nrx1β/NL1 ectodomains is highly negative at the postsynaptic side and much less so at the presynaptic side (Figure S5). It is intriguing to speculate that this "polarized" nature of the sheet-like structure positioned at the synaptic cleft may affect diffusion behavior of charged substances including neurotransmitters. The extent of this hypothetical "polarization" can be further modulated by the insertion of the highly basic (net charge of +8, Figure S1B) SpA sequence at the presynaptic face. Furthermore, the charge of the SpA sequence can be changed by alternative usage of two submodules, A1 and A2, found in humans and mice, where A1 corresponds to the rat SpA used here, and A2 is a highly acidic (net charge of −5) 20-residue segment (Comoletti et al., 2006).

Apart from the possible electrostatic effect described above, the clustered adhesion molecules can physically affect the mobility of other membrane proteins on the synaptic surface by acting like a picket fence. Because growing evidence suggests that the lateral diffusion behavior of neurotransmitter receptors affects synaptic activity (Bannai et al., 2009; Frischknecht et al., 2009; Heine et al., 2008; Zhao et al., 2008), the dynamic physical properties of the adhesion machinery made up of various components need to be investigated more rigorously. Some of the NL mutations associated with familial autism are mapped to the sites close to the interfaces implicated in sheet formation, but not the primary interface of the Nrx/NL binding (Figure S5) (Yan et al., 2005). These mutations may affect the size and the stability of the sheet, pointing toward possible

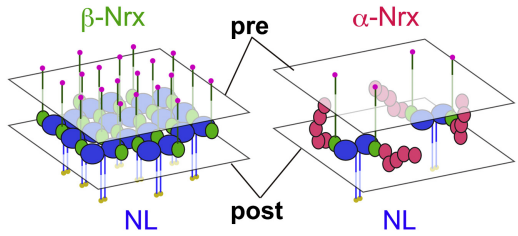

Figure 6. Hypothetical Clustering Modes for Nrx-NL Adhesion Complexes Based on Crystallographic and Electron Microscopic Observations

The globular acetylcholine esterase domain dimer of NL is represented by blue ovals, whereas the LNS6 domain of β-Nrx that interacts with NL is shown in small green ovals. In the case of α-Nrx, the LNS6 domain is preceded by the additional LNS1–LNS5 domains (red ovals), resulting in the larger ectodomain that is incompatible with the dense lateral packing of the complex. Stalk regions of both proteins connecting the globular ectodomain to membrane (translucent planes) are shown as straight lines, terminating with small spheres (gold for NL and pink for Nrx) that represent the PDZ binding motifs located at the C termini. See also Figure S5.

involvement of the extracellular architecture of synapses in higher-order function of neuronal circuit.

EXPERIMENTAL PROCEDURES

Expression Constructs

All the expression constructs for NL1 were made from full-length rat NL1 cDNA containing both SpA and SpB (pCMVNL1-14, a gift from T.C. Südhof) (Ichtchenko et al., 1996). For the soluble ectodomain construct used for crystallization, SpB (residues 298–306) was removed by overlapping extension PCR to yield the A^+B^- version of the ectodomain (residues 31–638), which was fused to the C terminus of human growth hormone (hGH) minigene in the pSGHV0 vector (Leahy et al., 2000). For cell surface expression of NL1, the DNA segment coding for EGFP derived from pEGFP-N3 (Clonetech) was inserted in-frame into a unique RsrII site located at the cytoplasmic tail of either the A^+B^+ or the A^+B^- version of full-length NL1 according to the strategy described by Sara et al. (2005). In addition all the cell surface NL1 constructs contained a FLAG tag at the N terminus, immediately after the signal sequence. To introduce unnatural N-glycosylation sequences at the multimer interfaces, the following two-residue mutations were introduced into each of three sites on separate NL1A^+B^+-EGFP constructs: S105N/I107T, D123N/R125S, and D140N/V142T.

All the expression constructs for Nrx1 were made from pCMV-N1a-1 (a gift from T.C. Südhof) (Ichtchenko et al., 1996) that codes for full-length bovine Nrx1α containing SS insertions at SS1, SS3, and SS5 but lacking SS2 and SS4. For the expression of soluble ectodomain fragment of Nrx1β, a region corresponding to the sixth LNS domain (residues 83–290 of Nrx1β, corresponding to residues 1,086–1,263 of Nrx1α) was PCR amplified and cloned in-frame into pGEX-HT, a version of pGEX-3T (GE Healthcare) modified to include an octahistidine tag and a TEV protease recognition site (Yasui et al., 2010). For cell surface expression of Nrx1α, a DNA fragment corresponding to the full-length Nrx1α was cloned into the pDsRed-monomer-N1 vector (Clonetech), yielding Nrx1α-DsRed that contains the monomeric version of a red fluorescent protein DsRed at the C terminus. The construct for Nrx1β-DsRed was prepared from that of Nrx1α-DsRed, by a series of extension PCR cycles, replacing the large N-terminal region containing the LNS1–LNS5 domains with a sequence unique to Nrx1β (residues 46–82). All Nrx1β constructs used in this study are the Δ variant that does not contain SS4.

Expression and Purification of Nrx1β and NL1

CHOlec3.2.8.1 cells (provided by P. Stanley) (Stanley, 1989) were cotransfected by electroporation with a plasmid encoding hGH-NL1A^+B^- together with a plasmid carrying a puromycin-resistance gene, plated on 96-well plates, and selected for resistance to 10 μg/ml puromycin. The cell clone with the highest expression level was selected and subjected to large-scale culture in media containing 2 μg/ml puromycin. The secreted protein was purified from the culture supernatant by Ni-NTA affinity chromatography, treated with histidine-tagged TEV protease, passed through Ni-NTA columns to remove cleaved hGH tag and His-tagged protease, and then further purified by anion-exchange chromatography on a Mono Q column (GE Healthcare). Nrx1β was overexpressed in *E. coli* cells as a glutathione S-transferase (GST) fusion protein and purified from bacterial lysate using a glutathione Sepharose 4B (GE Healthcare) affinity column. The fusion protein was treated with octahistidine-tagged TEV protease and passed through Ni-NTA columns to remove cleaved GST and TEV protease. Nrx1β was further purified by cation-exchange chromatography on a Mono S column (GE Healthcare).

Crystallization and Structural Analysis of the Nrx1β /NL1 Complex

For crystallization of the Nrx1β/NL1 complex, both purified proteins were dialyzed against 10 mM Tris-Cl (pH 8.0) and 0.1 M NaCl, mixed at a molar ratio of 1.1 (Nrx1β):1 (NL1), and concentrated to 10 mg/ml. Crystals of the complex were grown by vapor diffusion in hanging drops. The crystals were obtained by mixing 0.5 μl protein solution with 0.1 μl reservoir solution containing 3–5 mM $CaCl_2$ in 10 mM Tris-Cl (pH 8.0) and 0.1 M NaCl at 293 K. The crystals were treated with a solution containing 10 mM Tris-Cl (pH 8.0), 0.1 M NaCl, and 20% PEG400 for dehydration and cryoprotection, and were flash-frozen in liquid nitrogen. All diffraction data were collected using synchrotron radiation beamline BL-17A of Photon Factory (Tsukuba, Japan). Structural determination and refinement were conducted as described in Extended Experimental Procedures.

Analysis for the Nrx1 and NL1-Mediated Cell Adhesion

For the cell aggregation assay, cells expressing Nrx1β-DsRed, Nrx1α-DsRed, or NL1-EGFP were detached from culture dishes with 1 mM EDTA, washed, and resuspended in DMEM containing 10% FBS at a concentration of 1.0×10^6 cells/ml. Equal volumes of Nrx1-DsRed and NL1-EGFP cell suspensions were mixed and incubated for 30 min at room temperature. The resulting cell mixtures were transferred onto 18 mm glass coverslips coated with 0.1 mg/ml poly-L-lysine, incubated for 20 min at room temperature, and then fixed with 4% formaldehyde. After washing, the coverslips were mounted on a glass slide with VECTASHIELD (Vector Labs, Burlingame, CA, USA). Fluorescence images were obtained using either a digital epifluorescence microscope (BZ-9000; Keyence, Osaka, Japan) or a confocal scanning laser microscope (LSM 5 EXCITER; Carl Zeiss, Jena, Germany).

CLEM Analysis for Nrx1 and NL1-Mediated Cell Adhesion at Sites of Heterophilic Cell-Cell Contact

The "Live Cell Kit" (composed of a finder grid, a Live Cell carrier, and a sapphire disc; available from Leica Microsystems) was assembled and placed at the bottom of a cell culture dish. Prior to assembly the sapphire discs were precoated with carbon at ~20 nm thickness, followed by coating with 0.01% poly-L-lysine to facilitate cell attachment. Suspensions of Nrx1-DsRed- and NL1-EGFP-expressing cells coincubated as described in the previous section were mounted on the sapphire discs, incubated for 20 min at room temperature, and fixed with 4% formaldehyde. After washing with a buffer containing 20 mM Na-K-phosphate (pH 7.4) and 0.15 M NaCl, fluorescence images of cells were recorded by a digital light microscope (Keyence BZ-9000), and immediately flash-frozen at 2,000–2,100 bar using a Leica EM PACT2 system. For the freeze substitution the samples were transferred to a Leica EM AFS system (Leica, Vienna). Cells were first treated with 0.2% tannic acid in anhydrous acetone at −85°C for 24 hr, followed by treatment with anhydrous acetone containing 2% (w/v) OsO_4 for an additional 24 hr at −85°C. The temperature was then slowly increased to −20°C at a warming rate of 9.3°C/hr. After keeping the temperature at −20°C for 5 hr, the samples were brought to 4°C at a rate of 8°C/hr. The substituted samples were rinsed several times with acetone and subjected to a two-step epoxy-resin infiltration protocol involving incubation with 50% resin for 12 hr and with 100% resin for 12 hr at ambient temperature. Finally, the resin was polymerized by heating at 45°C for 1 day followed by additional heating at 60°C for 3 days.

The EM specimens were prepared from the resin-embedded samples as follows. First, the sapphire disc and the carrier were removed from the resin block. Using the finder grid located behind the cell layer as a reference, the area of interest was identified, and the surrounding regions were trimmed off with a razor blade. Semithin sections of 500–1,000 nm thickness were first excised and placed on a cover glass and observed under light microscope after staining with 0.5% (w/v) toluidine blue to check if the relative positions of cells were maintained during the fixation and embedding. Serial thin sections (70 nm thick) were then prepared from the remaining block and collected on EM copper grids. Thin sections were stained with 2.5% uranyl acetate followed by Reynold's lead citrate. Thin-section images were recorded at 20,000× magnification with an H-7650 electron microscope (Hitachi) equipped with a 1 × 1k CCD camera (TVIPS) and operated at an acceleration voltage of 80kV. When higher magnifications (e.g., 40,000× and 80,000×) were required for the quantitative analyses of the intermembrane distances, an H9500SD microscope (Hitachi) equipped with a 2 × 2k CCD camera (TVIPS) operated at an acceleration voltage of 200kV was used.

SUPPLEMENTAL INFORMATION

Supplemental Information includes Extended Experimental Procedures and five figures and can be found with this article online at http://dx.doi.org/10.1016/j.celrep.2012.06.009.

LICENSING INFORMATION

ACKNOWLEDGMENTS

We thank Hyota Takamatsu and Atsushi Kumanogoh for helping with the confocal laser microscopy, Norihisa Yasui for helpful discussions and experimental advice, Keiko Tamura-Kawakami, Emiko Mihara, and Maiko Nampo for their excellent technical support, Mayumi Nakano for preparation of the manuscript, Samuel Thompson for editing the manuscript, and Takeshi Uemura and Tomas C. Südhof for helpful comments on the manuscript. We are also grateful to the staff of the beamlines at Photon Factory (Tsukuba, Japan) and SPring-8 (Harima, Japan) for providing data collection facilities and support. This work was supported in part by the Grant-in-Aid for Scientific Research (A) from the Ministry of Education, Culture, Sports, Science and Technology of Japan (MEXT), by the Protein 3000 Project grant from MEXT, and by the Grant-in-Aid for Scientific Research on Innovative Areas (Transient macromolecular complex) from MEXT.

Received: February 13, 2012
Revised: May 7, 2012
Accepted: June 11, 2012
Published online: July 19, 2012

REFERENCES

Araç, D., Boucard, A.A., Ozkan, E., Strop, P., Newell, E., Südhof, T.C., and Brunger, A.T. (2007). Structures of neuroligin-1 and the neuroligin-1/neurexin-1 beta complex reveal specific protein-protein and protein-Ca2+ interactions. Neuron *56*, 992–1003.

Bannai, H., Lévi, S., Schweizer, C., Inoue, T., Launey, T., Racine, V., Sibarita, J.B., Mikoshiba, K., and Triller, A. (2009). Activity-dependent tuning of inhibitory neurotransmission based on GABAAR diffusion dynamics. Neuron *62*, 670–682.

Boucard, A.A., Chubykin, A.A., Comoletti, D., Taylor, P., and Südhof, T.C. (2005). A splice code for trans-synaptic cell adhesion mediated by binding of neuroligin 1 to alpha- and beta-neurexins. Neuron *48*, 229–236.

Brown, E., Mantell, J., Carter, D., Tilly, G., and Verkade, P. (2009). Studying intracellular transport using high-pressure freezing and Correlative Light Electron Microscopy. Semin. Cell Dev. Biol. *20*, 910–919.

Chen, F., Venugopal, V., Murray, B., and Rudenko, G. (2011). The structure of neurexin 1α reveals features promoting a role as synaptic organizer. Structure *19*, 779–789.

Chen, X., Liu, H., Shim, A.H., Focia, P.J., and He, X. (2008). Structural basis for synaptic adhesion mediated by neuroligin-neurexin interactions. Nat. Struct. Mol. Biol. *15*, 50–56.

Chih, B., Gollan, L., and Scheiffele, P. (2006). Alternative splicing controls selective trans-synaptic interactions of the neuroligin-neurexin complex. Neuron *51*, 171–178.

Comoletti, D., Flynn, R.E., Boucard, A.A., Demeler, B., Schirf, V., Shi, J., Jennings, L.L., Newlin, H.R., Südhof, T.C., and Taylor, P. (2006). Gene selection, alternative splicing, and post-translational processing regulate neuroligin selectivity for beta-neurexins. Biochemistry *45*, 12816–12827.

Dalva, M.B., McClelland, A.C., and Kayser, M.S. (2007). Cell adhesion molecules: signalling functions at the synapse. Nat. Rev. Neurosci. *8*, 206–220.

Dean, C., and Dresbach, T. (2006). Neuroligins and neurexins: linking cell adhesion, synapse formation and cognitive function. Trends Neurosci. *29*, 21–29.

Dean, C., Scholl, F.G., Choih, J., DeMaria, S., Berger, J., Isacoff, E., and Scheiffele, P. (2003). Neurexin mediates the assembly of presynaptic terminals. Nat. Neurosci. *6*, 708–716.

Fabrichny, I.P., Leone, P., Sulzenbacher, G., Comoletti, D., Miller, M.T., Taylor, P., Bourne, Y., and Marchot, P. (2007). Structural analysis of the synaptic protein neuroligin and its beta-neurexin complex: determinants for folding and cell adhesion. Neuron *56*, 979–991.

Frischknecht, R., Heine, M., Perrais, D., Seidenbecher, C.I., Choquet, D., and Gundelfinger, E.D. (2009). Brain extracellular matrix affects AMPA receptor lateral mobility and short-term synaptic plasticity. Nat. Neurosci. *12*, 897–904.

Graf, E.R., Zhang, X., Jin, S.X., Linhoff, M.W., and Craig, A.M. (2004). Neurexins induce differentiation of GABA and glutamate postsynaptic specializations via neuroligins. Cell *119*, 1013–1026.

Gray, E.G. (1975). Synaptic fine structure and nuclear, cytoplasmic and extracellular networks: the stereoframework concept. J. Neurocytol. *4*, 315–339.

Heine, M., Groc, L., Frischknecht, R., Béïque, J.C., Lounis, B., Rumbaugh, G., Huganir, R.L., Cognet, L., and Choquet, D. (2008). Surface mobility of postsynaptic AMPARs tunes synaptic transmission. Science *320*, 201–205.

Ichtchenko, K., Nguyen, T., and Südhof, T.C. (1996). Structures, alternative splicing, and neurexin binding of multiple neuroligins. J. Biol. Chem. *271*, 2676–2682.

Koehnke, J., Jin, X., Trbovic, N., Katsamba, P.S., Brasch, J., Ahlsen, G., Scheiffele, P., Honig, B., Palmer, A.G., 3rd, and Shapiro, L. (2008). Crystal structures of beta-neurexin 1 and beta-neurexin 2 ectodomains and dynamics of splice insertion sequence 4. Structure *16*, 410–421.

Koehnke, J., Katsamba, P.S., Ahlsen, G., Bahna, F., Vendome, J., Honig, B., Shapiro, L., and Jin, X. (2010). Splice form dependence of beta-neurexin/neuroligin binding interactions. Neuron *67*, 61–74.

Leahy, D.J., Dann, C.E., 3rd, Longo, P., Perman, B., and Ramyar, K.X. (2000). A mammalian expression vector for expression and purification of secreted proteins for structural studies. Protein Expr. Purif. *20*, 500–506.

Lisé, M.F., and El-Husseini, A. (2006). The neuroligin and neurexin families: from structure to function at the synapse. Cell. Mol. Life Sci. *63*, 1833–1849.

Lucić, V., Yang, T., Schweikert, G., Förster, F., and Baumeister, W. (2005). Morphological characterization of molecular complexes present in the synaptic cleft. Structure *13*, 423–434.

McDonald, K.L. (2009). A review of high-pressure freezing preparation techniques for correlative light and electron microscopy of the same cells and tissues. J. Microsc. *235*, 273–281.

Miller, M.T., Mileni, M., Comoletti, D., Stevens, R.C., Harel, M., and Taylor, P. (2011). The crystal structure of the α-neurexin-1 extracellular region reveals a hinge point for mediating synaptic adhesion and function. Structure *19*, 767–778.

Missler, M., and Südhof, T.C. (1998). Neurexins: three genes and 1001 products. Trends Genet. *14*, 20–26.

Peters, A., Palay, S.L., and Webster, H.D. (1991). Fine Structure of the Nervous System: Neurons and Their Supporting Cells, Third Edition (New York: Oxford University Press).

Plitzko, J.M., Rigort, A., and Leis, A. (2009). Correlative cryo-light microscopy and cryo-electron tomography: from cellular territories to molecular landscapes. Curr. Opin. Biotechnol. *20*, 83–89.

Polishchuk, R.S., Polishchuk, E.V., Marra, P., Alberti, S., Buccione, R., Luini, A., and Mironov, A.A. (2000). Correlative light-electron microscopy reveals the tubular-saccular ultrastructure of carriers operating between Golgi apparatus and plasma membrane. J. Cell Biol. *148*, 45–58.

Rudenko, G., Nguyen, T., Chelliah, Y., Südhof, T.C., and Deisenhofer, J. (1999). The structure of the ligand-binding domain of neurexin Ibeta: regulation of LNS domain function by alternative splicing. Cell *99*, 93–101.

Sara, Y., Biederer, T., Atasoy, D., Chubykin, A., Mozhayeva, M.G., Südhof, T.C., and Kavalali, E.T. (2005). Selective capability of SynCAM and neuroligin for functional synapse assembly. J. Neurosci. *25*, 260–270.

Scheiffele, P., Fan, J., Choih, J., Fetter, R., and Serafini, T. (2000). Neuroligin expressed in nonneuronal cells triggers presynaptic development in contacting axons. Cell *101*, 657–669.

Sheckler, L.R., Henry, L., Sugita, S., Südhof, T.C., and Rudenko, G. (2006). Crystal structure of the second LNS/LG domain from neurexin 1alpha: Ca2+ binding and the effects of alternative splicing. J. Biol. Chem. *281*, 22896–22905.

Shen, K.C., Kuczynska, D.A., Wu, I.J., Murray, B.H., Sheckler, L.R., and Rudenko, G. (2008). Regulation of neurexin 1beta tertiary structure and ligand binding through alternative splicing. Structure *16*, 422–431.

Stanley, P. (1989). Chinese hamster ovary cell mutants with multiple glycosylation defects for production of glycoproteins with minimal carbohydrate heterogeneity. Mol. Cell. Biol. *9*, 377–383.

Südhof, T.C. (2008). Neuroligins and neurexins link synaptic function to cognitive disease. Nature *455*, 903–911.

Tanaka, H., Nogi, T., Yasui, N., Iwasaki, K., and Takagi, J. (2011). Structural basis for variant-specific neuroligin-binding by α-neurexin. PLoS One *6*, e19411.

Ullrich, B., Ushkaryov, Y.A., and Südhof, T.C. (1995). Cartography of neurexins: more than 1000 isoforms generated by alternative splicing and expressed in distinct subsets of neurons. Neuron *14*, 497–507.

Verkade, P. (2008). Moving EM: the Rapid Transfer System as a new tool for correlative light and electron microscopy and high throughput for high-pressure freezing. J. Microsc. *230*, 317–328.

Yan, J., Oliveira, G., Coutinho, A., Yang, C., Feng, J., Katz, C., Sram, J., Bockholt, A., Jones, I.R., Craddock, N., et al. (2005). Analysis of the neuroligin 3 and 4 genes in autism and other neuropsychiatric patients. Mol. Psychiatry *10*, 329–332.

Yasui, N., Nogi, T., and Takagi, J. (2010). Structural basis for specific recognition of reelin by its receptors. Structure *18*, 320–331.

Zhao, J., Peng, Y., Xu, Z., Chen, R.Q., Gu, Q.H., Chen, Z., and Lu, W. (2008). Synaptic metaplasticity through NMDA receptor lateral diffusion. J. Neurosci. *28*, 3060–3070.

Zuber, B., Nikonenko, I., Klauser, P., Muller, D., and Dubochet, J. (2005). The mammalian central nervous synaptic cleft contains a high density of periodically organized complexes. Proc. Natl. Acad. Sci. USA *102*, 19192–19197.